ACS NANO

www.acsnano.org

ARTICLE

2D Vanadium Sulfides: Synthesis, Atomic Structure Engineering, and Charge Density Waves

Camiel van Efferen,* Joshua Hall, Nicolae Atodiresei, Virginia Boix, Affan Safeer, Tobias Wekking, Nikolay A. Vinogradov, Alexei B. Preobrajenski, Jan Knudsen, Jeison Fischer, Wouter Jolie, and Thomas Michely

Cite This: *ACS Nano* 2024, 18, 14161−14175

Read Online

ACCESS | Metrics & More | Article Recommendations | Supporting Information

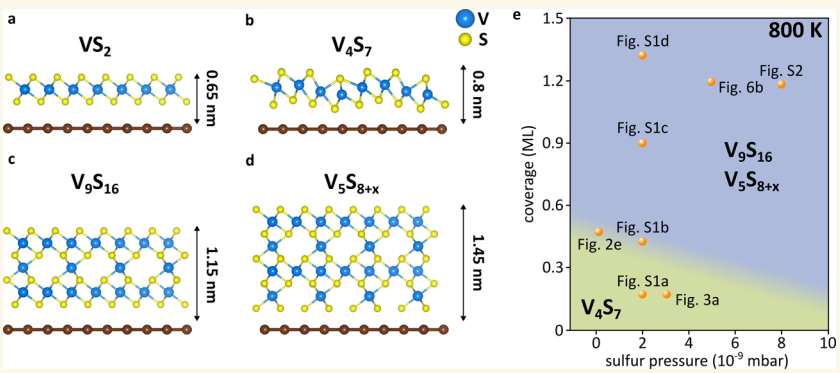

ABSTRACT: **Two ultimately thin vanadium-rich 2D materials based on VS_2 are created via molecular beam epitaxy and investigated using scanning tunneling microscopy, X-ray photoemission spectroscopy, and density functional theory (DFT) calculations. The controlled synthesis of stoichiometric single-layer VS_2 or either of the two vanadium-rich materials is achieved by varying the sample coverage and sulfur pressure during annealing. Through annealing of small stoichiometric single-layer VS_2 islands without S pressure, S-vacancies spontaneously order in 1D arrays, giving rise to patterned adsorption. Via the comparison of DFT calculations with scanning tunneling microscopy data, the atomic structure of the S-depleted phase, with a stoichiometry of V_4S_7, is determined. By depositing larger amounts of vanadium and sulfur, which are subsequently annealed in a S-rich atmosphere, self-intercalated ultimately thin V_5S_8-derived layers are obtained, which host 2 × 2 V-layers between sheets of VS_2. We provide atomic models for the thinnest V_5S_8-derived structures. Finally, we use scanning tunneling spectroscopy to investigate the charge density wave observed in the 2D V_5S_8-derived islands.**

KEYWORDS: *transition metal dichalcogenides, VS_2, V_5S_8, charge density wave, layer dependence, atomic structure engineering, 2D materials*

Atomic structure engineering of two-dimensional (2D) materials in order to tailor their electronic and chemical properties has been on the forefront of recent research. Various methods to achieve this have been explored, like the introduction of point or line defects,[1−3] creating horizontal or vertical heterostructures,[4,5] doping or gating,[6−9] as well as intercalation of native or foreign atoms between the layers.[10,11]

The creation of defects has been particularly successful in engineering transition metal dichalcogenides (TMDCs).[12] Chalcogen vacancies alone can be used to dope TMDCs[13] to develop or enhance a magnetic ground state[14,15] or to gain increased surface reactivity.[16,17] Vacancies can be created by extrinsic means like electron beam irradiation[13,18] but can also spontaneously form under suitable conditions through thermal annealing.[15,16]

Received: June 29, 2023
Revised: April 18, 2024
Accepted: April 30, 2024
Published: May 21, 2024

https://doi.org/10.1021/acsnano.3c05907
ACS Nano 2024, 18, 14161−14175

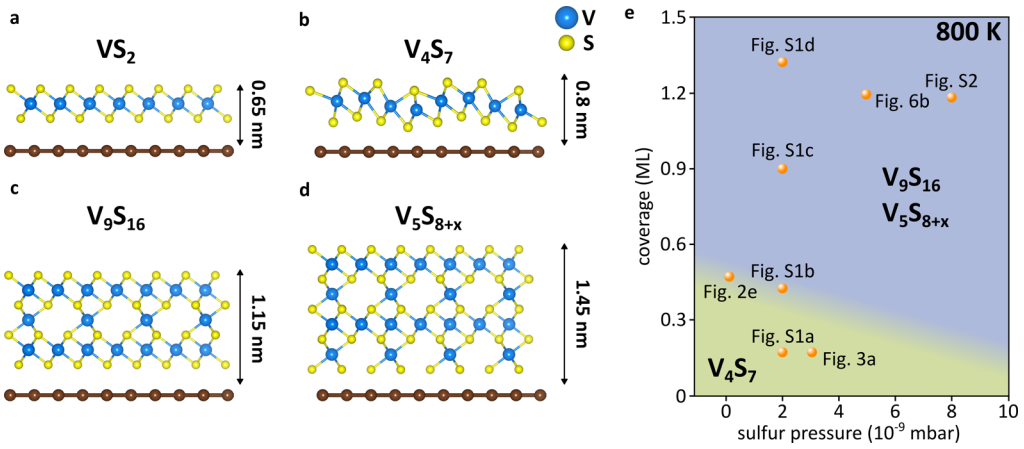

Figure 1. Atomic structures and phase diagram of VS_x compounds. (a–d) Atomic structure models of VS_2, V_4S_7, V_9S_{16}, and V_5S_{8+x}, respectively. Below the structures, a Gr substrate layer is drawn; besides the images, the apparent height measured with STM is indicated. The suggested structure of V_4S_7 is based on density functional theory (DFT) calculations. For V_5S_{8+x}, the actual configuration of the S atoms in the lowest layer is not known. (e) Schematic representation of phases present after an annealing temperature of 800 K. The figures indicated next to data points represent the corresponding compounds. Figures S1 and S2 are in the Supporting Information. With increasing initial coverage and annealing S pressure, the transition of VS_2 into V_4S_7 is suppressed. Instead, a 2 × 2 self-intercalated material is obtained, with stoichiometry V_9S_{16} or V_5S_{8+x} depending on the number of intercalation layers.

Since TMDCs are layered materials, they are also easily intercalated, with additional metal atoms placed between the TMDC sheets.[11] Intercalated atomic layers have been used to enhance electronic conductivity and induce ferromagnetism, phase transitions, or Ising superconductivity in TMDCs.[19−23] While these intercalants have been used extensively to intercalate bulk TMDCs,[10,19,21,22] recently the focus has shifted to bilayer TMDC intercalation, being the thinnest intercalated material.[20,24,25]

Among TMDCs, vanadium-based compounds like VS_2 have attracted substantial theoretical research interest due to their predicted electronically correlated and magnetic ground states when thinned down to a single layer.[26−29] However, due to the lack of a stable bulk polymorph,[30,31] VS_2 is a particularly challenging material to synthesize as a few-layer system, and it was a late addition of the single-layer TMDCs when it was synthesized on Au(111)[32] and on quasi-freestanding on Gr/Ir(111), where a $9 \times \sqrt{3}R30^\circ$ charge density wave (CDW) was found.[33] Owing to the wealth of experiments performed on VS_2 and its sister compound VSe_2 showing the absence of net magnetic moment in these materials, it is commonly accepted that the theoretically predicted ferromagnetic ground state[26−29] is not realized in pristine single layers of these materials.[15,33,34]

In contrast, the stable compound, V_5S_8, exhibits layer-dependent magnetism, which transforms with decreasing thickness from antiferromagnetic to ferromagnetic.[35−37] These results have so far been limited to samples down to 3 nm thickness since this compound has not yet been realized in its minimum thickness configuration of two VS_2 layers sandwiching a 2 × 2 V intercalation layer. Transport measurements of bulk V_5S_8 show no increase in the resistivity at low temperatures, suggesting that it does not have a CDW,[38,39] though upon cooling down to 100 K, an anisotropic contraction of V−V bonds was observed using X-ray diffraction.[40] Several studies also note that the magnetic moment of the intercalated V atoms can couple to the itinerant electrons in the VS_2 sheets, leading to the Kondo effect.[41,42]

Here, we explore two 2D vanadium−sulfide compounds, created using a two-step molecular beam epitaxy process. The synthesis consists of an initial growth step at room temperature and an annealing step at elevated temperature to enhance island shape and alignment. Depending on the amount of deposited material during growth, the temperature, and the S pressure during annealing, three materials of different V/S stoichiometries are obtained. Since V deposition always takes place in large S excess, the deposited amount is characterized through the amount of V deposited—the V atoms stay on the surface, while excess S evaporates. The unit used is monolayer (ML), which characterizes the V amount needed to grow a full single layer of stoichiometric VS_2, i.e., an amount of 1.12×10^{19} V atoms per m^2. The synthesis is performed in each case on the inert graphene Gr/Ir(111) substrate. 2D materials on this substrate were proven to be quasi-freestanding due the single crystal quality of the Gr layer and the negligible hybridization with Gr.[43−45] Specifically, the excellent agreement between experiment and theory for the properties of CDWs in the single-layer materials of TaS_2, VS_2, and NbS_2 indicates an at most weak substrate effect on the formation and properties of CDWs in single-layer 2D materials on Gr/Ir(111).[33,46,47] Transfer of the 2D vanadium−sulfide compounds on insulating substrates using standard techniques like polydimethylsiloxane stamps[48] for subsequent investigations is straightforward.

Single-layer islands of stoichiometric and phase-pure VS_2 are obtained when less than 0.5 ML are deposited at room temperature and annealed to a temperature not exceeding 600 K.[33] Under these conditions, the resulting single-layer VS_2 is always present in the 1T phase, as depicted in Figure 1a. When stoichiometric VS_2 is exposed to higher annealing temperatures, it gradually transforms into V_4S_7, a process that is completed at an annealing temperature of ≈800 K. V_4S_7 has periodically arranged rows of S vacancies and an accompanying buckling of the lattice, see Figure 1b. However, when the initial coverage during growth is larger, specifically when the islands resulting from the initial growth carry second layer islands of significant size, a different compound is formed upon annealing. It consists of layers of VS_2 self-intercalated with V atoms in a 2 × 2 pattern. The bulk stoichiometry of this phase would be V_5S_8, which has a NiAs structure with ordered V vacancies every second layer (leaving a quarter of the V atoms to form the 2 × 2 pattern).[49]

https://doi.org/10.1021/acsnano.3c05907
ACS Nano 2024, 18, 14161−14175

Table 1. Overview of Vanadium Sulfide Compounds and Their Synthesis Parameters

growth parameters and properties of vanadium sulfide compounds				
stoichiometry	VS_2	V_4S_7	V_9S_{16}	V_5S_{8+x}
coverage (ML)	≤0.5	≤0.5	>0.5	>0.5
annealing temperature (K)	≤600	≈800	≈800	≈800
annealing S pressure (mbar)	$0-8 \times 10^{-9}$	$0-8 \times 10^{-9}$	5×10^{-9}	5×10^{-9}
purity	phase pure	phase pure	not phase pure, mixed with other V_5S_8-derived structures	not phase pure, dominant with excess V
CDW, T_c	$(9 \times \sqrt{3})R30°$, >300 K	none, none	$(\sqrt{3} \times \sqrt{3})R30°$, ≈110 K	$(\sqrt{3} \times \sqrt{3})R30°$, ≈110 K
structure	T-phase TMDC	S-vacancy rows	2 × 2-intercalation, V_5S_8-derived	2 × 2-intercalation, V_5S_8-derived
apparent height (nm)	0.65	0.8	1.15	1.45
figure	2d	2f	5b	6d

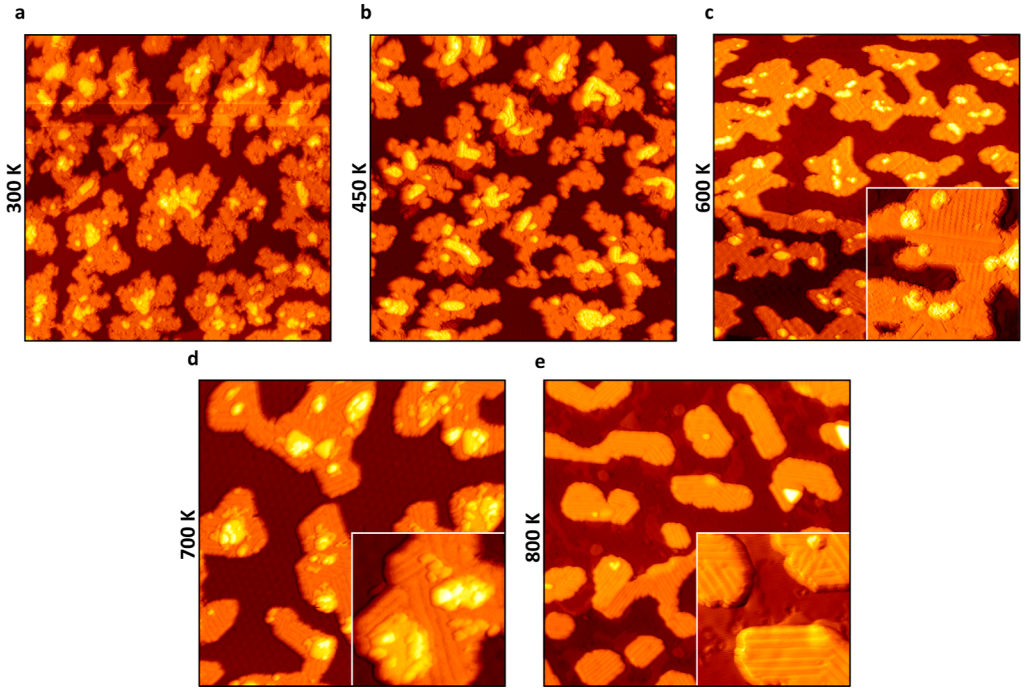

Figure 2. Evolution of stoichiometric VS_2 with temperature. (a) STM topograph of VS_2 islands with a coverage of 0.5 ML directly after growth at 300 K. (b–e) STM topographs after annealing to the indicated temperatures. The insets in (c–e) are close-ups of the topographs, highlighting the different superstructures. All annealing was performed without S background pressure. Images taken at 300 K. To enhance the visibility of the structures, each image displayed is a superposition of constant current STM topograph and its derivative. Image information (image size, sample bias, and tunneling current): main panels 80 × 80 nm^2, inset 20 × 20 nm^2. (a) −1.0 V, 210 pA; (b) −1.0 V, 90 pA; (c) −1.0 V, 100 pA, inset: −0.7 V, 550 pA; (d) −1.2 V, 110 pA, inset: −1.2 V, 110 pA; and (e) −1.3 V, 10 pA, inset: −1.3 V, 10 pA.

The V/S ratio of bulk V_5S_8 is a limit reached only when the number of layers goes to infinity. We obtain V_5S_8-derived islands of minimal thickness, consisting of two layers of VS_2 with a 2 × 2 layer of V atoms intercalated in the van der Waals (vdWs) gap between the layer. Consequently, the stoichiometry is V_9S_{16}, see Figure 1c. We also find evidence for the presence of a doubly intercalated structure. In that case, a second 2 × 2 layer of V, passivated by S atoms, intercalated in the vdWs gap between the bottom VS_2 sheet and Gr, as depicted in Figure 1d. We denote this structure as V_5S_{8+x} since the precise amount of S saturating the V is unknown. To show the different growth regimes in S pressure and coverage needed to obtain either the vacancy row structure V_4S_7 or the 2D derivatives of V_5S_8, a schematic representation is shown in Figure 1e, wherein the structures obtained after room-temperature growth and subsequent annealing at a temperature of 800 K are collected.

In this study, the materials shown schematically in Figure 1 are investigated using scanning tunneling microscopy (STM), X-ray photoemission spectroscopy (XPS), and DFT calculations. Furthermore, using low-temperature scanning tunneling spectroscopy (STS), a $(\sqrt{3} \times \sqrt{3})R30°$ CDW is found in the 2D V_5S_8-derived islands, with a transition temperature below 110 K. An overview of our results is given in Table 1.

RESULTS

Creating 1D-Patterned V_4S_7 from Single-Layer VS_2. In Figure 2a, the sample topography directly after growth at room temperature is shown. Dendritic first layer islands of 0.65 nm apparent height are visible, covered by small second layer islands. After annealing under vacuum to 450 K, see Figure 2b, the single-layer islands are less rough, but dendritic shapes are still prevalent. After annealing to 600 K, in Figure 2c, the islands are more compact with smoother edges. A superstructure, identified in a previous work as a unidirectional charge density wave with an approximate unit cell of $9 \times \sqrt{3}$R30°,[33] covers all

https://doi.org/10.1021/acsnano.3c05907
ACS Nano 2024, 18, 14161−14175

but the smallest regions of the islands. The CDW appears only after annealing to 600 K, as its formation requires sufficiently large islands of stoichiometric VS_2. The instability of the CDW on small islands of VS_2 has been documented in a previous work.[33]

Further annealing to 700 K, see Figure 2d, leads to the dominant presence of a different type of striped superstructure (note that already at 600 K, some stripes are present, compare Figure 2c). The dark stripes have nonuniform spacing with a minimal width of ≈1 nm and several domains of different orientations, as can be seen in the inset. After annealing to 800 K, in Figure 2e, the VS_2 islands are elongated but compact and display a well-ordered pattern of stripes. The stripes are generally aligned with the island edges and exhibit only three domains, rotated by 120°. The islands have an altered apparent height of 0.8 nm (see Note 3 of the Supporting Information for line profiles of the relevant topographies). The area of the islands has decreased—correspondingly, patches of what are presumably S and V atoms intercalated under the Gr are visible. Annealing beyond 800 K leads to the formation of higher structures, discussed below, and elongated crystallites which are not studied in the present manuscript, see Note 4 of the Supporting Information.

Focusing on the stripe superstructure, Figure 3a shows the result of annealing the stripes to 800 K in a moderate sulfur

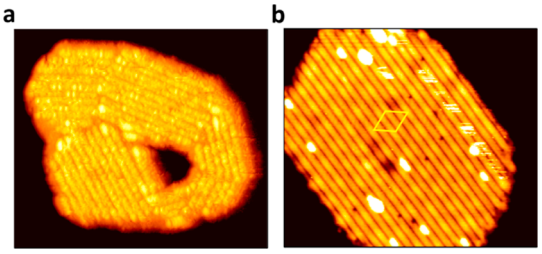

Figure 3. Patterned adsorption of S on striped superstructure. (a) STM topograph of a V_4S_7 island with dark stripes covered by adsorbates after annealing in a S-rich environment to 800 K. (b) STM topograph of island surface after quick heating to 600 K. Most of the adsorbates have desorbed. The yellow rhombus indicates the Gr/Ir(111) moiré unit cell shining through the V_4S_7 island. Note that the example island shown in (b) is not the same island as in (a). Images taken at 300 K. Image information (image size, sample bias, and tunneling current): (a) 35 × 30 nm², −0.5 V, 10 pA; (b) 30 × 30 nm², −0.3 V, 20 pA.

background of $P^{a}_{sulfur} = 2 \times 10^{-9}$ mbar. Bright stripes of adsorbates are present on the island, with a spacing corresponding to the periodicity of the superstructure. Subsequent annealing largely removes the adsorbates uncovering the superstructure again, as shown in Figure 3b. Only some bright adsorbate clusters are left. The moiré of Gr/Ir(111) (marked with a yellow rhombus) becomes apparent again after annealing.

We interpret the situation as follows: upon cooldown from the annealing step, residual S, which is hard to pump out, adheres to the islands. The subsequent brief heating in clean UHV causes desorption of these adsorbed S atoms. Irrespective of the details, the observations imply a modulated reactivity of the stripe superstructure. Note that for stoichiometric VS_2 islands, such structured adsorption was never observed. Note also the reconstructed island edges in Figure 3b, with the stripes causing kinked edges in segments parallel and orthogonal to them. The stripe superstructure being imprinted on the step edge highlights that the structure is not of electronic but of structural origin.

Turning to the atomic structure of the stripes, Figure 4a shows an atomically resolved image of the surface of a striped single-layer island. The rectangular unit cell is shown as a black box. Its dimensions are (3.20 ± 0.05) Å along its short axis and (9.1 ± 0.1) Å along its long axis. The line profile along the black line shows an apparent height corrugation of about 0.4 Å. Depending on the tunneling conditions, the apparent height varied in the range from 0.4 to 0.6 Å. The STM contrast allows identification of two rows of atoms (presumably S atoms separated by grooves with a faint substructure.)

Assuming the superstructure to result from S desorption and given the rectangular symmetry of the unit cell with an S atom at each corner of the unit cell, it would be compatible with a VS_2 lattice from which either every second or every fourth row of S desorbed. If this would occur without any other changes in the bonding distances of the V and lower S layer, one would expect a periodicity of either $2 \times a_{VS2} \times \sqrt{3}/2 = 5.5$ Å or $4 \times a_{VS2} \times \sqrt{3}/2 = 11.1$ Å normal to the removed rows. While the periodicity resulting from the removal of every second S row is inconsistent with the measured unit cell dimension, the somewhat larger unit cell size derived from our assumption of every fourth S row removed could be rationalized by a bond order−bond length argument: the remaining atoms strengthen their bonds and consequently shorten them.

A model involving the removal of every fourth row was also proposed for a similar sized unit cell with the same symmetry by Liu et al.[16] for the sister compound, VSe_2. They observed a striped phase after annealing monolayer VSe_2 grown on graphite.

To clarify the situation, we conducted DFT calculations confining VS_2 to the size of the experimental unit cell. We placed the VS_2 layer on Gr and removed every fourth top layer S row. After relaxation, the structure shown in Figure 4b,c was obtained. The nominal composition of the compound is V_4S_7. The removal of the S atom row has led to a buckling of the structure and changed the coordination of one of the remaining rows of S atoms from 3-fold to 4-fold. The simulated STM image shown in Figure 4d, using precisely the same sample bias of −0.5 V as in the experiment, shows striking agreement with the experimental topograph of Figure 4a. The predicted corrugation of the structure of ≈0.6 Å matches reasonably well with experiment, as does the asymmetry of the profile.

Giving up the constraint of an initially intact VS_2 layer with just S rows removed, alternative models can be considered. If an additional VS_2 unit is removed per cell, compound V_3S_5 is formed by bond reorganization. Simulated STM topographs reproduce the experimental STM contrast reasonably well (compare Note 5 of the Supporting Information). However, the corrugation of the resulting structure is well above 2 Å, at variance with experiment. Its formation would furthermore involve bond breaking and either loss V or expansion of islands, which are also considered to be unlikely. A model similar to this scenario was proposed by Chua et al.[15] to explain a striped phase after annealing of monolayer VSe_2 on MoS_2. However, their unit cell was substantially larger and of different symmetry than the S compound discussed here.

In order to obtain additional information about the effect of annealing stoichiometric VS_2, we performed high-resolution X-ray photoemission spectroscopy (XPS) of the S 2p core level. Figure 5a shows the S 2p core-level spectra obtained for samples

https://doi.org/10.1021/acsnano.3c05907
ACS Nano 2024, 18, 14161−14175

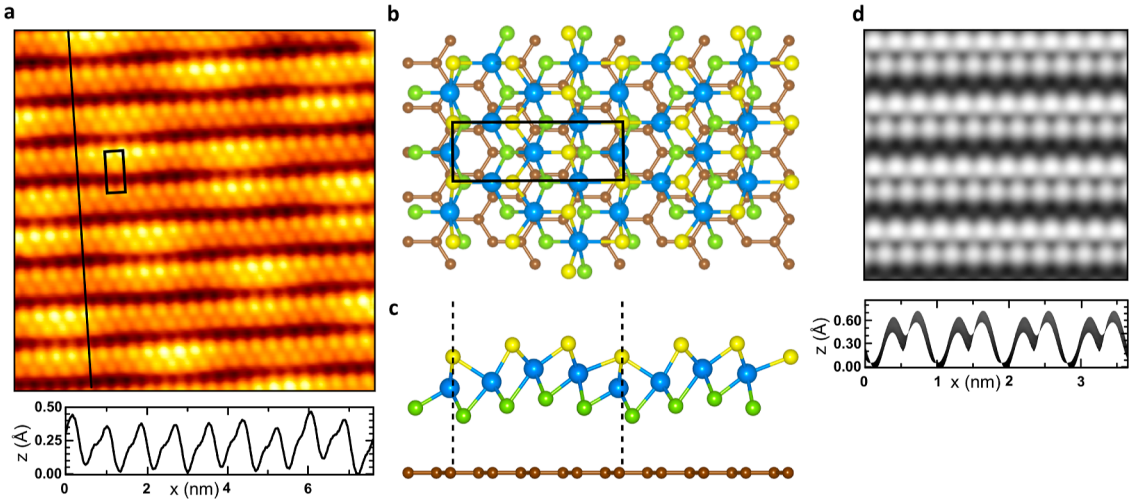

Figure 4. Reconstruction of VS_2 into V_4S_7 through defect row formation. (a) Atomically resolved STM topograph of the stripes. The unit cell of the dominant striped superstructure (black) is indicated. The black line indicates the position of the line profile. (b,c) Top and side view of structural model of S-deficient VS_2 on graphene obtained by DFT calculations. Note that the black box that indicates the unit cell is rotated 90° with respect to the STM image depicted in (a). The bottom S atoms are colored green to allow for easy identification when viewed from the top. (d) Simulated STM image (isosurface of the charge density) at −0.5 V. Below, the isosurface is shown from the side, so the corrugation can be seen. Image taken at 1.7 K. Image information (image size, sample bias, and tunneling current): (a) 7.5 × 7.5 nm^2, −0.5 V, 1.4 nA.

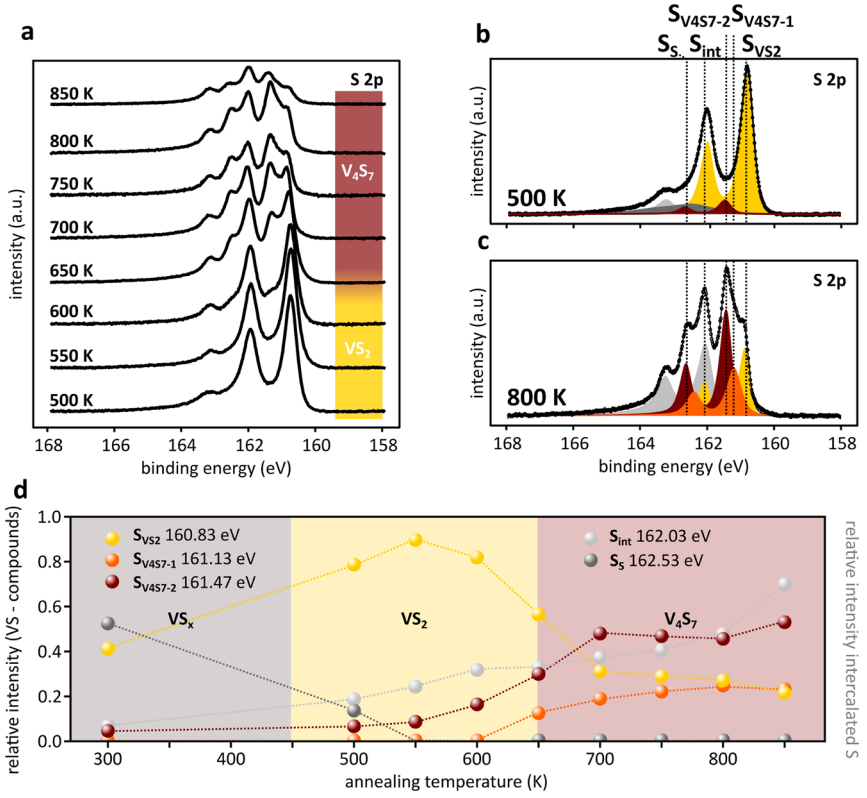

Figure 5. XPS of single-layer VS_2. (a) Temperature-resolved X-ray photoemission spectra (XPS) of S $2p_{3/2}$ and S $2p_{1/2}$ core-level spectra of VS_2 with a coverage of 0.5 ML measured at a photon energy of $h\nu$ = 260 eV. For each successive data point, the sample was annealed to the indicated temperature without additional S and then measured at 300 K. (b,c) XPS spectra of S 2p core-level spectra fitted with 5 components. The fitted components are denoted as S_{VS_2} (yellow), S_{V4S7-1} and S_{V4S7-2} (orange and brown), S_{int} (silver), and S_S (dark gray), see text for discussion. The data points are represented by black circles and the overall fit by a solid black line. (d) Change of the relative intensities of the fit components during the entire annealing sequence as a function of temperature. Dashed lines to guide the eye. Note that the relative intensity of the intercalated S atoms S_{int} has been plotted on the right *y*-axis versus the total S signal of the atoms in the vanadium compound.

with increasing annealing temperatures in the absence of S pressure from bottom to top. Spin−orbit coupling of the S 2p level gives rise to an S $2p_{3/2}$ and S $2p_{1/2}$ doublet separated by 1.19(3) eV. At 500 K, only a single S 2p doublet is visible, with peaks at 160.83(3) and 162.02(3) eV. As the annealing temperature is increased, more doublets become pronounced.

https://doi.org/10.1021/acsnano.3c05907
ACS Nano 2024, 18, 14161−14175

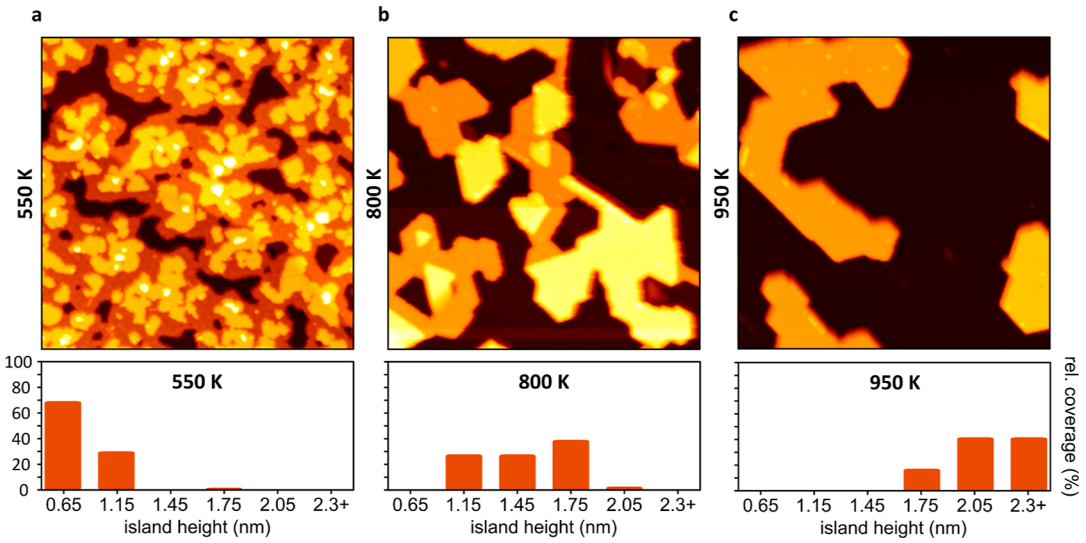

Figure 6. Evolution of multiheight VS_x with temperature. (a) STM topograph after deposition of ≈1.2 ML, annealed at 550 K in a S-rich atmosphere. (b) STM topograph after annealing to 800 K. (c) STM topograph after annealing to 950 K. Below the STM topographs in (a−c), histograms of the relative coverage of islands of different apparent heights are shown. Images taken at 4−7 K. STM parameters: (a−c) 80 × 80 nm^2, (a) 1.0 V, 50 pA, (b) −1.0 V, 50 pA, and (c) 1.0 V, 100 pA.

In particular, the S 2p peak intensities shift toward higher binding energies. At the highest annealing temperature of 850 K, the total intensity of the signal is significantly reduced.

Fitting the XPS spectra across the whole range of annealing temperatures requires five doublets, which will be discussed by reference to the lower binding energy $2p_{3/2}$ peak of the doublet. In Figure 5b, a single component (160.83(3) eV, yellow) dominates the spectrum, denoted as S_{VS2}. In contrast, the 800 K spectrum in Figure 5c is made up of multiple doublets of similar intensity. Crucially, two doublets close to the original yellow component are now present at 800 K, which we denote as S_{V4S7-1} (161.13(3) eV, orange) and S_{V4S7-2} (161.47(3) eV, brown). Comparison to the 500 K spectrum furthermore reveals that the dark gray (162.53(3) eV) component S_S has disappeared, whereas the silver (162.03(3) eV) component S_{int} is still present and has larger relative intensity.

From STM images, we know that at or below 600 K, mainly unperturbed (though defective) single-layer VS_2 islands are present (compare Figure 2a−c). We therefore assign S_{VS2} to stoichiometric VS_2. S_S, which disappears rapidly when the sample is heated up from room temperature, we assign to sulfur species which react or desorb upon annealing. S_{int}, on the other hand, can be straightforwardly assigned to S atoms intercalated between Gr and Ir(111).[50] The presence of intercalated S atoms is inferred from STM images (see Note 6 of the Supporting Information) and low-energy electron diffraction (LEED), an example of which is shown in Figure 7. The assignment is further based on the presence of this peak at the same location for all samples investigated in this study. Its high binding energy furthermore sets it apart from the peaks intrinstic to the vanadium sulfide compound. S_{V4S7-1} and S_{V4S7-2} finally are related to the formation of the striped vacancy row V_4S_7 observed in STM, as these components are present in significant intensity only at higher annealing temperatures.

Plotting the relative intensities of all components against the annealing temperature in Figure 5d, we can broadly distinguish three stages. At 300 K, stoichiometric VS_2 is coexisting with unreacted sulfur (compare Figure 2a and Note 7 of the Supporting Information). Upon annealing to 500 K, the sulfur desorbs from the surface, leaving a sample consisting mainly of stoichiometric VS_2, with about 90% of the vanadium sulfide intensity stemming from the S_{VS2} component. Above 600 K, the sample undergoes a transition to V_4S_7, with S_{V4S7-1} and S_{V4S7-2} becoming prominent with a ratio that tends to 1:2. Because of this ratio, we assign S_{V4S7-2} to the two almost equivalent, 3-fold coordinated S atom rows in the DFT calculation of Figure 4b,c, and S_{V4S7-1} to the other S atom row, which has a 4-fold coordination, see Note 8 of the Supporting Information. While S_{VS2} is reduced in intensity and shifts to a slightly higher binding energy by ≈100 meV when the sample is annealed, it remains present up to 800 K, when the sample surface uniformly exhibits the striped superstructure. We infer that this signal stems from the bottom S atoms, which are in a chemical environment not too different to that of pristine VS_2. At higher annealing temperatures, the S detached from VS_2 intercalates below Gr, which can be seen in Figure 2e, leading to the strong increase in the relative intensity of the S_{int} component.

In conclusion, we interpret V_4S_7 to emerge gradually with increasing annealing temperature through loss of sulfur from the initial VS_2 islands and an accompanying reconstruction of the atomic lattice (compare Figures 2c−e). At about 800 K, the density of the vacancy rows has reached a saturation, resulting in uniform V_4S_7 characterized by every fourth sulfur top layer row missing. The XPS spectra, which show the appearance of S 2p doublets at considerably higher binding energies, support this interpretation. In particular, the presence of extra S 2p components indicates that most of the top layer S atoms are in a different chemical environment compared to pristine VS_2, which makes a different stoichiometry likely. The loss in S is accompanied by a substantial lattice reconstruction, also consistent with the reshaping of the islands, which reflect the vacancy row periodicity. In contrast, no significant changes are observed in the V 2p XP spectra, see Note 9 of the Supporting Information.

The observation of a striped sulfur-depleted phase after annealing of a monolayer of VS_2 or VSe_2 appears to be a common feature of these materials. However, the precise structure that is obtained depends on the substrate. Annealing of

https://doi.org/10.1021/acsnano.3c05907
ACS Nano 2024, 18, 14161−14175

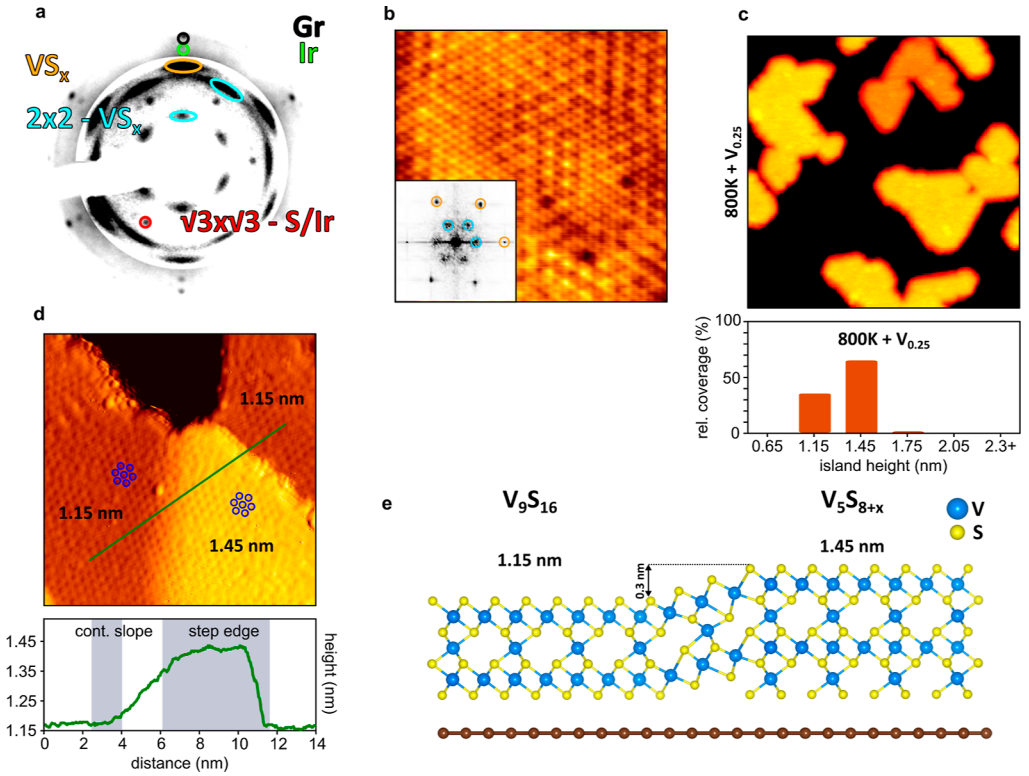

Figure 7. 2 × 2 self-intercalation in multiheight VS_x. A 118 eV LEED image of VS_x after annealing to 800 K. Some Gr and Ir first-order reflections are encircled black and green, respectively. Intercalated S (red) gives rise to a $\sqrt{3} \times \sqrt{3}$ superstructure with respect to Ir. Some first-order reflections of VS_x (orange) and reflections of a 2 × 2 superstructure with respect to VS_x (light blue) are encircled. The contrast of the inner part of the LEED image has been enhanced for clarity. (b) Room-temperature STM topograph of 1.15 nm island, with FFT as inset. A clear 2 × 2 superstructure is visible on the island. (c) STM topograph of the VS_x sample, where 25% additional V atoms were deposited on a sample with a coverage of ≈1.2 ML grown at 300 K and annealed to 500 K. After room-temperature V deposition, the sample was subsequently annealed to 800 K in UHV (no S pressure). (d) STM topograph of 1.15 and 1.45 nm islands on sample without additional V atoms. A $(\sqrt{3} \times \sqrt{3})R30°$ superstructure is highlighted with blue circles on both islands, see text. Below the topograph, a height profile taken long the green line is shown. (e) Side view of atomic structure model of 1.15 and 1.45 nm islands forming a continuous top layer. STM parameters: (b) 300 K, 10 × 10 nm^2, −1.0 V, and 200 pA; (c) 110 K, 80 × 80 nm^2, 1.5 V, and 550 pA; and (d) 77 K, 16 × 16 nm^2, −1.0 V, and 200 pA.

VS_2 on graphite results in V_4Se_7, as observed by Liu et al.;[16] similarly, annealing of VS_2 on graphene results in V_4S_7, as observed by us. Despite the difference in the chalcogen, the same stoichiometry and very similar structures with a rectangular unit cell and an orthorhombic 2D Bravais lattice are formed. Although annealing of VSe_2 on MoS_2 as done by Chua et al.[15] leads to the same stoichiometry of V_4Se_7, the unit cell is oblique and the symmetry is that of a monoclinic 2D Bravais lattice. Finally, annealing of monolayer VS_2 on Au(111), as conducted by Arnold et al.[32] and Kamber et al.,[51] results in a more S-depleted stoichiometry of V_2S_3, which in addition has a quite different internal structure of the cell. It would display single rows of S atoms rather than the double rows as observed experimentally and simulated by DFT (compare Figure 4).

The formation of chalcogen vacancy rows or line defects due to annealing, electron, or laser beam irradiation seems furthermore a general feature in TMDCs like MoS_2, $MoTe_2$, and WS_2.[52−55] In the specific case of single-layer VSe_2, annealing-induced Se-vacancy rows were used to lift the spin frustration of the material, leading to room-temperature ferromagnetism.[15] Since the CDW ground state responsible for the magnetic frustration[56] is very similar in both stoichiometric single layers of VS_2 and VSe_2, it would be of great interest to track the effect of annealing VS_2 on its magnetic properties. In contrast to VSe_2, however, where it is possible to transform the patterned state back to stoichiometric VSe_2 via low-temperature annealing after deposition of Se atoms,[15,16] low-temperature annealing in sulfur vapor did not recreate stoichiometric VS_2 from V_4S_7. Depending on the coverage of the sample, either adsorbed S atoms on top of the patterned material were observed, depicted in Figure 4d, or—in the case of larger coverage—higher structures were obtained, which will be discussed below.

Self-Intercalation of V Atoms in Multilayer VS_2. Instead of single-layer VS_2 or V_4S_7, we can selectively grow a different 2D material by changing the growth conditions to favor higher structures. Already during growth at 300 K, multilayer structures form (see Figure 2a). As we deposit more material, a substantial fraction of the material will grow on top of single-layer VS_2. When we then anneal in a S-rich environment to about 800 K, structures with several height levels are created, which do not manifest S vacancies in their top layer.

In Figure 6a−c, the evolution of such a sample is depicted. After annealing ≈1.2 ML of VS_x to 550 K, the apparent height distribution shows the 0.65 nm apparent height characteristic for single-layer VS_2, a significant area fraction of 1.15 nm height and some small areas of 1.75 nm apparent height, as shown in Figure 6a. Annealing the sample to 800 K leads to a transformation of island shapes and apparent heights, shown in Figure 6b. The island edges are straight, largely aligned to the dense-packed

https://doi.org/10.1021/acsnano.3c05907
ACS Nano 2024, 18, 14161−14175

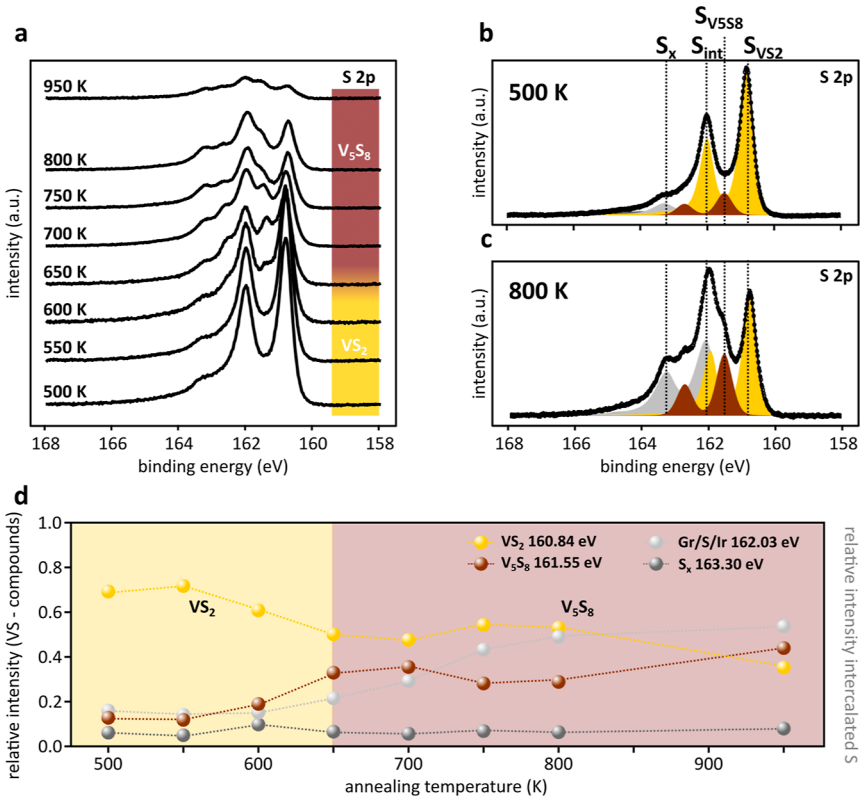

Figure 8. XPS of multiheight VS_x. (a–c) Temperature-resolved X-ray photoemission spectra (XPS) of the S $2p_{3/2}$ and S $2p_{1/2}$ core levels of VS_2 with a coverage of ≈1.2 ML measured at a photon energy of $h\nu$ = 260 eV. For each spectrum, the sample was annealed to the indicated temperature in a S background pressure of 3×10^{-9} mbar and then measured at 300 K. The XPS spectra are fitted with 4 components. The fitted components are S_{VS2} (yellow), S_{V5S8} (brown), S_{int} (silver), and S_x (dark gray), see text for discussion. The data points are represented by black circles and the overall fit by a solid black line. (d) Change of the relative intensities of the fit components as a function of temperature. Dashed lines are present to guide the eye. Note that the relative intensity of the intercalated S atoms S_{int} has been plotted on the right *y*-axis versus the total S signal of the atoms in the vanadium compound.

directions of Gr. Two additional island apparent heights (1.45 and 2.05 nm) appear, both 0.3 nm offset from the higher islands already present at 550 K. The lowest islands are now 1.15 nm high. No single-layer VS_2 is present on the surface. While the different islands are generally sharply demarcated by step edges from one another, continuous transitions between them are also observed, like in the bottom left of Figure 6b. These transitions will be discussed below. When the sample is further annealed to 950 K, as shown in Figure 6c, only islands with apparent heights of 1.75 nm and up are observed. We thus find that as the annealing temperature increases, the island density goes down, while the average apparent island height increases, with island heights separated by ≈0.3 nm. The resulting sample cannot be understood as multilayer VS_2 since the height of each VS_2 layer is ≈0.6 nm. We therefore refer to these samples as multiheight VS_x. Our investigation will focus on the lower two levels of 1.15 and 1.45 nm apparent height, which will be identified as 2D derivates of V_5S_8.

In the LEED pattern of the multiheight sample annealed at 800 K, where the apparent minimum island height is 1.15 nm, we find multiple ordered structures, see Figure 7a. The Gr (black circle) and iridium (green circle) first-order spots are visible, surrounded by hardly visible satellite spots from their moiré. Closer to the center, sharp $\sqrt{3} \times \sqrt{3}$ spots with respect to Ir [$(\sqrt{3} \times \sqrt{3})_{Ir}$] are present, which stem from S intercalation under Gr. The VS_x spots (orange ellipses) are elongated, indicating a small epitaxial spread in orientation angles, which sets them apart from the perfectly oriented spots of the substrate. Besides the first-order VS_x spots, two other sets of spots with the same elongation are visible, which are identified as first- and second-order spots of a 2×2 superstructure with respect to VS_x. The first-order spots indicate a hexagonal symmetry with a lattice parameter of 3.23 ± 0.03 Å. This is close to the lattice parameter of stoichiometric VS_2 (3.21 ± 0.02 Å).[33,57] However, the strong 2×2 reflections are characteristic of V_5S_8, a material of monoclinic symmetry which can be understood as a bulk crystal consisting of sheets of VS_2 with a 2×2 layer of V atoms in between.[49]

An atomically resolved STM topograph, taken at room temperature, of a 1.15 nm high island after annealing to 800 K, depicted in Figure 7b, shows that the material has preserved its hexagonal symmetry on the surface—as expected from the LEED pattern. At room temperature and under favorable imaging conditions, along with the atomic lattice, a 2×2 superstructure is visible. The superstructure is slightly disordered. This is also evident in the fast Fourier transform (FFT) shown in the inset of Figure 7b, where the 2×2 spots (green circles) are broader than the atomic lattice spots (yellow circles). The presence of a (2×2) superstructure in STM is consistent with a 2×2 intercalation layer, as expected for V_5S_8. The fact that it is hard to image and not present on all atomic resolution topographs obtained indicates that the 2×2 layer does not originate from the top layer, again as expected for an intercalation layer in a V_5S_8-derived structure.

https://doi.org/10.1021/acsnano.3c05907
ACS Nano 2024, 18, 14161–14175

To confirm that it is straightforward to self-intercalate V into existing layers, we evaporated 25% additional V atoms on an already grown VS_x sample annealed to 500 K. Prior to V deposition, the sample was comparable to the sample shown in Figure 6a, with uncovered single-layer VS_2 and some islands of 1.15 nm apparent height. The evaporation was performed in UHV, with no additional S added. After deposition, the sample was annealed to 800 K in UHV—so again without the addition of any S. The result is shown in Figure 7c. Compared to Figure 6b, which was annealed to the same temperature, the ratio of 1.45 nm islands to 1.15 nm islands has increased, and little to no thicker layers have formed. Crucially, no V atoms or clusters are present on top of the islands or the Gr. The V atoms have been incorporated in the islands, changing their stoichiometry. In the LEED of this sample, a clear 2 × 2 signal can be distinguished, consistent with our interpretation of a 2 × 2 intercalation structure, see Note 10 of the Supporting Information.

No structural differences exist between the surfaces of the 1.15 and 1.45 nm islands. On the contrary, a continuous transition from one island type to the other is possible, as evinced in Figure 7d. In the image, an island of 1.45 nm apparent height can be seen to continuously transform into the island of 1.15 nm on the right-hand side, while a step edge separates it from the 1.15 nm island in the upper left, as can be seen in the line profile below Figure 7d. Because of this continuity, we conclude that the structure of the islands is essentially the same.

The thinnest possible form of V_5S_8 consists of two layers of VS_2 intercalated by a single 2 × 2 sheet of V atoms and has a stoichiometry of V_9S_{16}, see Figure 1c. The second thinnest 2D V_5S_8 derivative would then have a second intercalation layer under the lower S atoms. With these structures in mind, we give an atomic model that explains the continuity in Figure 7e. Since V atoms below the island would be highly reactive, we presume that they are passivated by S atoms. This additional layer of V and S accounts for the 3 Å apparent height difference between the islands, see in Figure 7e. The stoichiometry of the thicker island, with two V intercalation layers, is dubbed V_5S_{8-x}, since the exact configuration of the bottom S atoms is not known. In conclusion, after annealing to 800 K, no multilayer VS_2 is present but only V_9S_{16}- or V_5S_8-derived layers which can be regarded as VS_2 multilayers with all van der Waals gaps intercalated with a 2 × 2 pattern of V atoms.

Using XPS, we investigated the S 2p core level of VS_x at different temperatures during an annealing experiment in a S-rich atmosphere corresponding to the STM sequence in Figure 6. The result is displayed in Figure 8a. After annealing to 500 K, the S_{VS2} doublet at 160.83(3) and 162.02(3) eV is most prominent in the spectrum, indicating the dominant presence of stoichiometric VS_2, see Figure 8b. When the annealing temperature is increased, S_{VS2} decreases in intensity, and a doublet S_{V5S8} appears at the higher binding energy of 161.55(3) eV (brown in Figure 8c). The total intensity of the signal is reduced significantly. However, unlike the annealing sequence in Figure 5, where a small coverage of VS_2 was annealed without S pressure, the S_{VS2} component in Figure 8 remains dominant up to 800 K. When we fit the spectra, using the same fitting parameters for S_{VS2} and S_{int} as for the fits of Figure 5, we find that we obtain a reliable fit for a total of four peaks. Besides S_{V5S8}, we added a minor dark gray component S_x located at 163.30(10) eV, hardly visible in the spectra and of unknown origin. Additional XP spectra of the sample with extra V atoms, shown in Figure 7c, can be found in Note 11 of the Supporting Information.

Tracking the relative intensities of all components in Figure 8d, it becomes apparent that S_{V5S8} is already present at the lowest investigated temperature and grows at the expense of S_{VS2}, with an onset for the growth between 550 and 600 K. S_x remains of equal low intensity throughout the annealing process, while S_{int} grows as the annealing temperature is increased.

We interpret the two characteristic components in V_5S_8-derived islands to stem from S atoms in two different chemical environments. S atoms bound only to 3 V neighbors as in VS_2 give rise to the S_{VS2} component, which undergoes a small shift on the order of ≈100 meV toward lower binding energies upon intercalation, while S atoms next to the V 2 × 2 intercalation layer, being bound to more than 3 V, give rise to the S_{V5S8} component. Although the 2 × 2 superstructure in STM and LEED alone could stem from a lattice distortion, the strong shift (≈700 meV) in the binding energy of the S atoms from the S_{VS2} to the S_{V5S8} doublet signals a more significant change in the chemical environment of the atoms. A similar shift to higher binding energy was observed in self-intercalated bilayers of VSe_2 in ref 58, where it was associated with a change in the electrostatic energy at the Se sites coordinated with more than 3 V atoms. Analogous to the XP spectra of V_5S_8, again no significant changes are observed in the V 2p XP spectra, see Note 12 of the Supporting Information.

Islands thicker than 1.45 nm are most likely also V_5S_8 derived. Consequently, the number of S atoms bordering 2 × 2 V planes increases upon annealing, causing the S_{V5S8} component to rise, while the number of surface S atoms decreases, leading to the decrease of the S_{VS2} component and the observed shift in relative ratio between the components. Since XPS is a surface-sensitive technique, the S_{VS2} component stemming from the top S atoms will generally outweigh the XPS signals of S atoms deeper in the islands, which explains the dominant presence of S_{VS2} even when most islands have one or more intercalation layers. We also cannot exclude the presence of (unintercalated/partially intercalated) vdWs gaps in the thicker islands. Their precise analysis lies beyond the scope of the manuscript.

Concerning the other components, the comparatively small increase in the relative intensity of S_{int}, compared to the increase of the same component in the XPS of single-layer VS_2, is probably due to the presence of S-intercalation already after annealing at 500 K since all annealing steps were performed in a S-rich environment (note the high intensity of the S intercalation spots in the LEED of Figure 7a). The increase in the intensity of S_{int} is thus a measure of the reduced surface area of the islands, exposing more of the Gr. The S_x component has little weight, and its origin cannot be conclusively determined. It could stem from adsorbed S since it has a similarly high binding energy as the S_S component in the monolayer.

To summarize at this point, we interpret the islands formed when annealing a large (>1 ML) deposited amount of VS_x in a S background pressure as being V_5S_8 derived. This is indicated by the simultaneous presence of a 2 × 2 superstructure in LEED and STM and the S_{V5S8} component in the S 2p XPS spectra, with a binding energy 700 meV higher than S_{VS2}. We are able to create a more pure minimal-thickness V_5S_8 sample via the evaporation of extra V atoms on a multiheight sample annealed to 500 K, and then annealing it to 800 K, as depicted in Figure 7c.

We note finally that in a similar fashion, V_5Se_8 was previously procured from seed layers of VSe_2 during thin film growth[59] or by increasing the substrate temperature during growth or annealing of single-layer VSe_2.[60,61] In a similar vein, the chemical vapor deposition growth of VS_2 nanosheets generally leads to

https://doi.org/10.1021/acsnano.3c05907
ACS Nano 2024, 18, 14161−14175

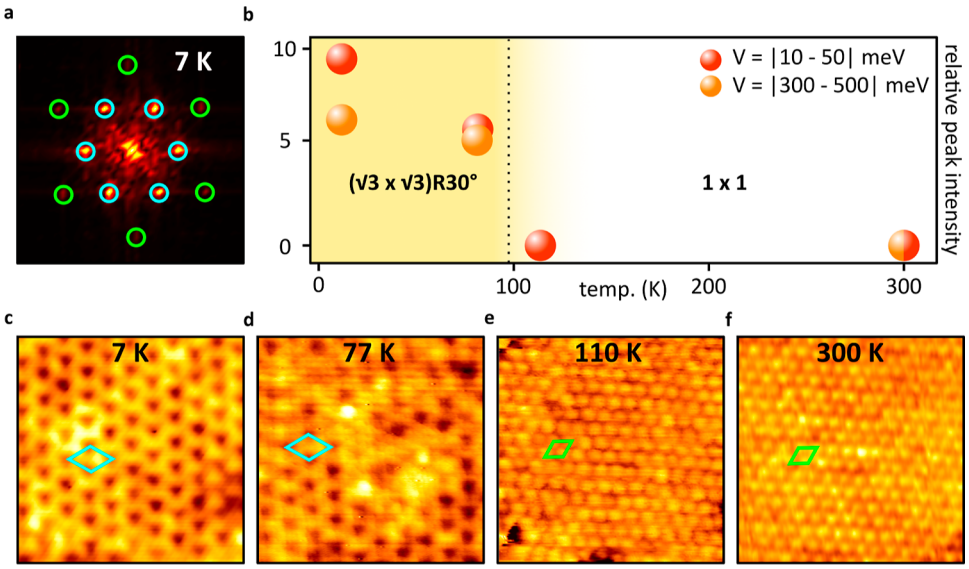

Figure 9. $(\sqrt{3} \times \sqrt{3})R30°$ CDW transition in thin V_5S_8-derived islands. (a) FFT of 1.15 nm V_9S_{16} island taken at 7 K, with the superstructure spots stemming from the $(\sqrt{3} \times \sqrt{3})R30°$ and atomic lattice encircled in cyan and green, respectively. (b) Temperature dependence of $(\sqrt{3} \times \sqrt{3})R30°$ CDW in V_9S_{16}. Thermal evolution of intensities of CDW peaks normalized to intensities of Bragg peaks, from FFTs of 5 × 5 nm^2 STM topographs of 1.15 nm (V_9S_{16}) and 1.45 nm high (V_5S_{8+x}) islands. (c–f) Topographs of the sample, as represented in the FFT of (a), taken at the indicated temperatures. The unit cells of the $(\sqrt{3} \times \sqrt{3})R30°$ (cyan) and the atomic lattice (green) are shown. The STM topographies used for the analysis were taken both close to the Fermi level (|10−50| meV) and far from it (|300−500| meV), to make certain that the disappearance is not an artifact stemming from different tunneling conditions. STM/STS parameters: (c–f) All topographs 5 × 5 nm^2; (c) −0.5 V, 50 pA; (d) −0.5 V, 200 pA; (e) 0.014 V, 500 pA; and (f) 0.010 V, 3 nA.

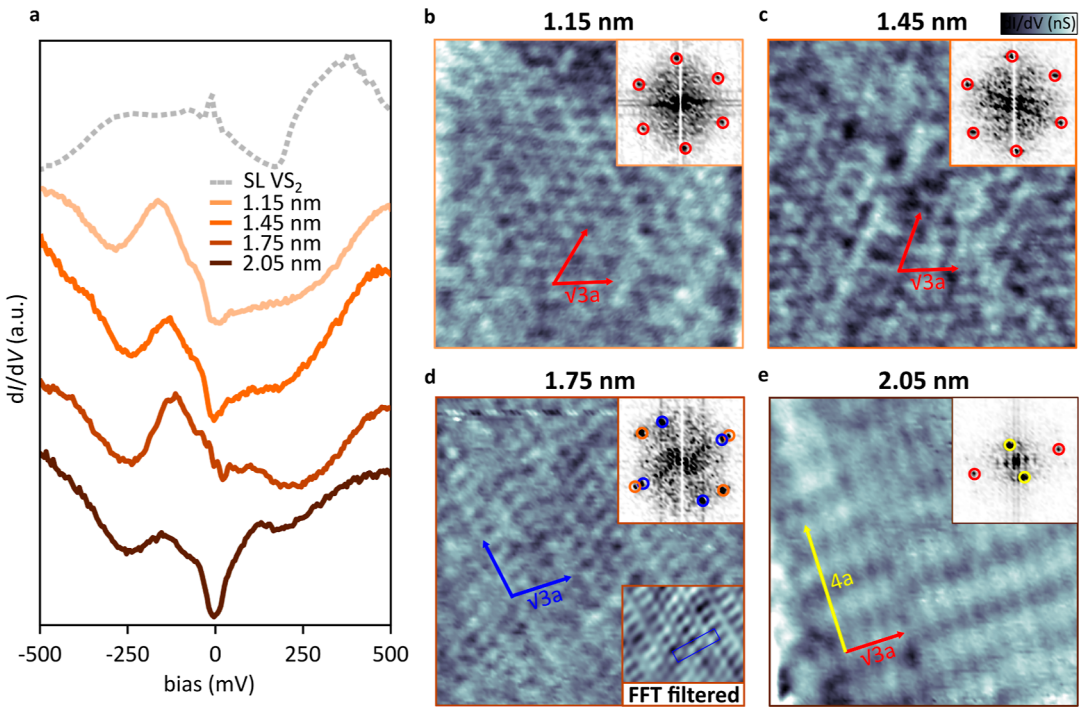

Figure 10. Multiple CDW orders in V_5S_8-derived islands. (a) dI/dV spectra of islands of different apparent heights. Spectrum of single-layer (SL) VS_2 (dashed line) added for comparison. (b–e) Constant-current dI/dV maps of different islands, all taken with V_{set} = −0.5 V. The insets show FFTs of the images. Note that the FFTs only display the superstructure; no atomic spots are present. The superstructure spots are encircled for emphasis. In the images, arrows are drawn to indicate the direction of particular periodicities. Each arrow has the size of three wavelengths of the corresponding structure. STM/STS parameters: (a) V_{stab} = −500 mV, I_{stab} = 250 pA; (b–e) 9 × 9 nm^2, −0.5 V, 100 pA. STS taken with f_{mod} = 871 Hz and V_{mod} = 5 mV. Maps obtained at 7 K.

the simultaneous presence of VS_2 and V_5S_8.[62,63] In each case, the small differences in formation energy between the self-intercalated material and the TMDC are emphasized. Here, we showed that providing extra V atoms after an initial growth step can help to favor one phase over the other and enables one to grow phase-pure ultrathin V_5S_8-derived materials down to the

https://doi.org/10.1021/acsnano.3c05907
ACS Nano 2024, 18, 14161−14175

minimal thickness of 1.15 nm. These minimal thickness islands with a stoichiometry of V_9S_{16} can be considered as single layers of a 2D material.

$(\sqrt{3} \times \sqrt{3})R30°$ CDW in Ultimately Thin V_5S_8-Derived Islands. When we cool down the multiheight sample, we find that the islands of 1.15 and 1.45 nm apparent height undergo a phase transition. In both island types, a pronounced superstructure with a periodicity of 5.5 ± 0.1Å $= \sqrt{3}\,a_{VS2}$ is observed in topography at temperatures ≤77 K. This superstructure can already be seen clearly in Figure 7d, where the $(\sqrt{3} \times \sqrt{3})R30°$ superstructure maxima are encircled in blue. It coexists with the CDW in the monolayer, see Note 13 of the Supporting Information.

Upon heating the sample from 7 K back to room temperature, the $(\sqrt{3} \times \sqrt{3})R30°$ superstructure vanishes and the atomic lattice becomes visible. As a measure of the strength of the superstructure, we take the relative peak intensity of the 1×1 Bragg peaks with respect to that of the $(\sqrt{3} \times \sqrt{3})R30°$ peaks.[64] In the 7 K FFT shown in Figure 9a, these are encircled in green and cyan, respectively. Plotting the relative intensities for FFTs obtained at different temperatures in Figure 9b, $(\sqrt{3} \times \sqrt{3})R30°$ can be seen to disappear between 77 and 110 K (see Note 14 of the Supporting Information for all topographies and FFTs). Some representative topographies are shown Figure 9c−f, which make clear that the 1×1 structure is recovered at 110 K. From the strong temperature dependence of the $(\sqrt{3} \times \sqrt{3})R30°$ superstructure, we conclude that it is likely a charge density wave. This CDW is not to be confused with the one that develops in single-layer VS_2, which is unidirectional and has a much higher transition temperature,[33] see Table 1 for the differences.

Finally, turning toward the electronic structure of the multiheight islands, we can see in Figure 10a that, in contrast to ML VS_2, which hosts a CDW with a full gap above the Fermi level E_F,[33] dI/dV spectra taken on the thinnest V_5S_8-derived islands (1.15 and 1.45 nm) show a partial gap around E_F, while a large density of states (DOS) peak is observed below E_F. Comparing the dI/dV spectra of islands of different apparent heights, taken with the same tip, we see essentially no differences between islands of 1.15 and 1.45 nm apparent height, which is in line with the fact that both have the same $(\sqrt{3} \times \sqrt{3})R30°$ CDW. While it is tempting to correlate the presence of a gap at the Fermi level with the CDW, a more thorough investigation, backed up by DFT calculations, is necessary to fully resolve this issue. Gaps at the Fermi level have also been argued to arise due to, e.g., inelastic tunneling effects,[65,66] whereas CDWs do not always lead to Fermi level gaps which can be resolved with STM.[33] In this case, temperature-resolved ARPES data could give more insight into the mechanism of CDW formation.

Investigating the electronic structure of the higher islands, we note that islands of 1.75 nm have a similar spectrum, with the same DOS peak below the Fermi level, albeit with a somewhat reduced gap around E_F and a more pronounced depression around 250 meV. At 2.05 nm apparent height, the center gap around E_F is deeper, and the peak and depression, below and above E_F, respectively, are less conspicuous. All in all, the differences between the spectra are small enough to consider all islands as representatives of the same generic V_5S_8 structure. This is in line with the LEED data, which does not show additional or different diffraction spots when the annealing temperature is increased.

dI/dV maps taken on the islands at 7 K, as shown in Figure 10b−e, reveal that the small differences in electronic structure can be correlated with different superstructures on the islands. Note that all maps shown are taken at the same bias voltage V_{set} = −0.5 meV, with the same tip, see Note 15 of the Supporting Information for an overview STM image showing all investigated islands. While the two lower islands both show the aforementioned $(\sqrt{3} \times \sqrt{3})R30°$, the lattice symmetry is broken in the higher islands, which exhibit striped superstructures. Upon closer inspection, the 1.75 nm superstructure can be understood as a $(\sqrt{3} \times \sqrt{3})R30°$ structure, together with dimerization along one of the high-symmetry directions of the lattice, which is highlighted in the inset of Figure 10d. The dimerization breaks the symmetry and leads to a distortion of the $\sqrt{3}a$ FFT spots. The superstructure of the 2.05 nm island shown in Figure 10e, on the other hand, can be readily decomposed into a $\sqrt{3}a$ and a $4a$ component, which are orthogonal to one another. We tentatively interpret these superstructures to be CDWs since LEED shows only 2×2 spots down to 40 K, so that structural rearrangements upon cooling down or different intercalation structures are less tenable as explanations. Nevertheless, a more comprehensive characterization is necessary to confirm the validity of our CDW interpretation.

The different superstructures illustrate the complexity of the system. They underscore both the ubiquity of CDWs and structural phase transitions in low-dimensional vanadium chalcogenides and the metastability of any particular periodicity. The situation seems to be analogous to the case of few-layer compounds of the vanadium-based materials VSe_2[67−71] and VTe_2,[72,73] which host a plenitude of CDW phases (e.g., 4×4, 4×1, $2\sqrt{3} \times 2\sqrt{3}$, 5×1, and $\sqrt{3} \times \sqrt{7}$), depending on the substrate and the number of layers.

With respect to V_5S_8 in particular, the fact that it hosts a CDW when thinned down to its 2D limit could be related to the layer dependence of its magnetism, which changes from antiferromagnetic to ferromagnetic when thinned down to 3.2 nm.[35−37] Since bulk V_5S_8 is not known to have a CDW, the interplay between the formation of the $(\sqrt{3} \times \sqrt{3})R30°$ CDW and the magnetic structure would be a compelling subject for further study.

CONCLUSIONS

In conclusion, we have grown and investigated two 2D vanadium-rich VS compounds: V_4S_7 and V_9S_{16}, the latter being the thinnest possible V_5S_8-derived material.

V_4S_7 is created from ML VS_2 by the formation of S-defects through annealing without additional sulfur vapor. At an annealing temperature of 800 K, the S defects have spontaneously ordered into a homogeneous array of 1D trenches. We have shown that this 1D pattern templates S adsorption and speculate that also other adsorbates can be templated through the vacancy row pattern. Based on the size and symmetry of the experimental unit cell, ab initio DFT calculations provided a stable structure model for V_4S_7, which is fully consistent with the STM data.

V_5S_8-derived islands are obtained automatically when a larger coverage (>0.5 ML) of VS_x is grown. At the investigated annealing temperatures, no multilayer VS_2 is present. Only V_9S_{16} or thicker V_5S_8-derived layers form, which can be considered to result from intercalation of all vdW gaps in multilayer VS_2 with a 2×2 V layer, forming a fully covalently bonded material. Using

https://doi.org/10.1021/acsnano.3c05907
ACS Nano 2024, 18, 14161−14175

low-temperature STM, the thinnest 2D V_5S_8-derived structures were shown to undergo a CDW transition to a $(\sqrt{3} \times \sqrt{3})R30°$ phase, which develops below 110 K, whereas the thicker islands were found to exhibit different superstructures, presumably all of CDW origin.

Our findings provide a recipe for the growth of two vanadium-rich single-layer vanadium compounds. Given the thickness-dependent magnetic and electronic properties of V_5S_8, having access to its 2D form is of particular interest for the further development of 2D magnetic materials.

METHODS

The experiments were conducted in five ultrahigh-vacuum systems (base pressure in the low 10^{-10} mbar range). Three systems were equipped with sample preparation facilities, scanning tunneling microscopy (STM)—operating at base temperatures given in the figure captions—and low-energy electron diffraction (LEED). The fourth system was the FlexPES beamline end station preparation chamber at MAX IV, Laboratory Lund, Sweden. There, the samples were grown following the same recipes as in the STM system, and sample quality was checked by LEED. The fifth system was an STM-only system, to which samples from FlexPES were transferred with a vacuum suitcase and then measured by STM at room temperature and 110 K.

Ir(111) was cleaned by cycles of noble gas sputtering (4.5 keV Xe^+ at 75° with respect to the surface normal or with 1 keV Ar^+ at normal incidence) and annealing to 1500 K. A closed monolayer of single-crystalline Gr on Ir(111) is grown by room temperature exposure of Ir(111) to ethylene until saturation, subsequent annealing to 1500 K, and followed by exposure to 200 L ethylene at 1200 K.[74]

The synthesis of vanadium sulfides on Gr/Ir(111) is based on a two-step molecular beam epitaxy approach introduced in detail in ref 43 for MoS_2. In the first step, the sample is held at room temperature, and V is evaporated at a rate of $F_V = 2.5 \times 10^{16}$ atoms m^{-2} s^{-1} into a sulfur background pressure of $P_S^g = 5 \times 10^{-9}$ mbar built up by thermal decomposition of pyrite inside a Knudsen cell. In a second step, the sample is annealed to 800 K with or without S pressure. The V flux was calibrated by STM from the coverage of single-layer VS_2 islands. In the captions, only the deposited V amount is specified as fraction of a monolayer (ML) where 1 ML is 1.12×10^{19} atoms m^{-2}, that is the amount of V in a full layer of VS_2 based on the measured lattice parameter of 3.21 Å.[33] For STM image processing, the WSxM software was used.[75]

The XPS experiments were conducted at the FlexPES beamline at MAX IV Laboratory, Lund, Sweden.[76] The growth of VS_x compounds at the beamline was conducted with a V evaporator calibrated by STM in the home lab. The calibration was confirmed through STM measurements of a sample prepared at the end station and transferred in a vacuum suitcase to the STM system at MAX IV. The S 2p core levels were measured with a photon energy of 260 eV. The measurements were conducted at room temperature with a spot size of 50 × 50 μm. The spectra for each sample were fitted simultaneously for all temperatures with pseudo-Voight functions. The width, skew, and ratio of Gaussian to Lorentzian contributions were fixed for each component, meaning that they were not allowed to vary between spectra taken at different annealing temperatures. The center energy of each component was granted a maximum deviation of ±100 meV to account for small shifts in the chemical environment between spectra while the intensities (total area) of the components were unconstrained. The fitting was performed with the lmfit module of python, using a basinhopping algorithm.

Our first-principles spin-polarized calculations were performed by using DFT[77] and the projector augmented plane wave method[78] as implemented in the VASP code.[79,80] For the plane wave expansion of the Kohn–Sham wave functions,[81] we used a cutoff energy of 500 eV. We performed the structural relaxation using vdW-DF2[82] with a revised Becke (B86b) exchange[83−85] functional to properly account for the nonlocal correlation effects like van der Waals interactions.[85] The analysis of the electronic structures was done by using the PBE exchange−correlation energy functional.[86]

ASSOCIATED CONTENT

Supporting Information

The Supporting Information is available free of charge at https://pubs.acs.org/doi/10.1021/acsnano.3c05907.

Transition from mono- to multilayer growth mode, formation of V_5S_8 at high S pressure, line profiles of VS_x islands, 1D crystallites of VS_x, DFT model of V_3S_5, S intercalation below Gr, S 2p XPS of VS_2 as grown, origin of S_{V4S7-1} and S_{V4S7-2} XPS components, V 2p XPS of V_4S_7, LEED of phase-pure V_5S_8-derived sample, S 2p XPS of multiheight VS_x, with 25% extra V, V 2p XPS of multiheight sample, single-layer VS_2 and V_9S_{16}, temperature dependence of $(\sqrt{3} \times \sqrt{3})R30°$ superstructure, and location of spectra and maps of multiheight sample (PDF)

AUTHOR INFORMATION

Corresponding Author

Camiel van Efferen − *II. Physikalisches Institut, Universität zu Köln, 50937 Köln, Germany;* orcid.org/0000-0002-6237-8602; Email: efferen@ph2.uni-koeln.de

Authors

Joshua Hall − *II. Physikalisches Institut, Universität zu Köln, 50937 Köln, Germany*

Nicolae Atodiresei − *Peter Grünberg Institut and Institute for Advanced Simulation, Forschungszentrum Jülich, 52428 Jülich, Germany*

Virginia Boix − *Division of Synchrotron Radiation Research, Department of Physics, Lund University, SE-221 00 Lund, Sweden;* orcid.org/0000-0002-1152-8201

Affan Safeer − *II. Physikalisches Institut, Universität zu Köln, 50937 Köln, Germany*

Tobias Wekking − *II. Physikalisches Institut, Universität zu Köln, 50937 Köln, Germany*

Nikolay A. Vinogradov − *MAX IV Laboratory, Lund University, SE-221 00 Lund, Sweden;* orcid.org/0000-0002-1477-853X

Alexei B. Preobrajenski − *MAX IV Laboratory, Lund University, SE-221 00 Lund, Sweden;* orcid.org/0000-0002-9444-7844

Jan Knudsen − *Division of Synchrotron Radiation Research, Department of Physics, Lund University, SE-221 00 Lund, Sweden; NanoLund, Department of Physics and MAX IV Laboratory, Lund University, SE-221 00 Lund, Sweden*

Jeison Fischer − *II. Physikalisches Institut, Universität zu Köln, 50937 Köln, Germany;* orcid.org/0000-0003-3538-1926

Wouter Jolie − *II. Physikalisches Institut, Universität zu Köln, 50937 Köln, Germany;* orcid.org/0000-0001-9319-3427

Thomas Michely − *II. Physikalisches Institut, Universität zu Köln, 50937 Köln, Germany;* orcid.org/0000-0003-1657-1847

Complete contact information is available at: https://pubs.acs.org/10.1021/acsnano.3c05907

Notes

The authors declare no competing financial interest.

https://doi.org/10.1021/acsnano.3c05907
ACS Nano 2024, 18, 14161−14175

ACKNOWLEDGMENTS

This work was funded by the Deutsche Forschungsgemeinschaft (DFG, German Research foundation) through CRC 1238 (project no. 277146847, subprojects A01, B06, and C01). V.B. and J.K. acknowledge the financial support from the Swedish Research Council (grant number 2017-04840, 2022-04363) and the Crafoord Foundation. We acknowledge MAX IV Laboratory for time on Beamline FlexPES under Proposal 20210859. Research conducted at MAX IV, a Swedish national user facility, is supported by the Swedish Research council under contract 2018-07152, the Swedish Governmental Agency for Innovation Systems under contract 2018-04969, and Formas under contract 2019-02496. The authors gratefully acknowledge the computing time granted by JARA Vergabegremium and provided on the JARA Partition part of the supercomputer JURECA at Forschungszentrum Jülich.

REFERENCES

(1) Ma, Q.; Isarraraz, M.; Wang, C. S.; Preciado, E.; Klee, V.; Bobek, S.; Yamaguchi, K.; Li, E.; Odenthal, P. M.; Nguyen, A.; et al. Postgrowth tuning of the bandgap of single-layer molybdenum disulfide films by sulfur/selenium exchange. *ACS Nano* **2014**, *8*, 4672−4677.

(2) Lin, Y.-C.; Björkman, T.; Komsa, H.-P.; Teng, P.-Y.; Yeh, C.-H.; Huang, F.-S.; Lin, K.-H.; Jadczak, J.; Huang, Y.-S.; Chiu, P.-W.; Krasheninnikov, A. V.; Suenaga, K. Three-Fold Rotational Defects in Two-Dimensional Transition Metal Dichalcogenides. *Nat. Commun.* **2015**, *6*, 6736.

(3) Coelho, P. M.; Komsa, H.-P.; Coy Diaz, H.; Ma, Y.; Krasheninnikov, A. V.; Batzill, M. Post-Synthesis Modifications of Two-Dimensional $MoSe_2$ or $MoTe_2$ by Incorporation of Excess Metal Atoms into the Crystal Structure. *ACS Nano* **2018**, *12*, 3975−3984.

(4) Huang, C.; Wu, S.; Sanchez, A. M.; Peters, J. J. P.; Beanland, R.; Ross, J. S.; Rivera, P.; Yao, W.; Cobden, D. H.; Xu, X. Lateral heterojunctions within monolayer $MoSe_2$−WSe_2 semiconductors. *Nat. Mater.* **2014**, *13*, 1096−1101.

(5) Vaňo, V.; Amini, M.; Ganguli, S. C.; Chen, G.; Lado, J. L.; Kezilebieke, S.; Liljeroth, P. Artificial heavy fermions in a van der Waals heterostructure. *Nature* **2021**, *599*, 582−586.

(6) Lin, Y.-C.; Dumcenco, D. O.; Huang, Y.-S.; Suenaga, K. Atomic mechanism of the semiconducting-to-metallic phase transition in single-layered MoS_2. *Nat. Nanotechnol.* **2014**, *9*, 391−396.

(7) Sutter, E.; Huang, Y.; Komsa, H.-P.; Ghorbani-Asl, M.; Krasheninnikov, A. V.; Sutter, P. Electron-beam induced transformations of layered tin dichalcogenides. *Nano Lett.* **2016**, *16*, 4410−4416.

(8) Wang, Y.; Xiao, J.; Zhu, H.; Li, Y.; Alsaid, Y.; Fong, K. Y.; Zhou, Y.; Wang, S.; Shi, W.; Wang, Y.; et al. Structural phase transition in monolayer $MoTe_2$ driven by electrostatic doping. *Nature* **2017**, *550*, 487−491.

(9) van Efferen, C.; Murray, C.; Fischer, J.; Busse, C.; Komsa, H.-P.; Michely, T.; Jolie, W. Metal-insulator transition in monolayer MoS_2 via contactless chemical doping. *2D Mater.* **2022**, *9*, 025026.

(10) Friend, R. H.; Yoffe, A. D. Electronic properties of intercalation complexes of the transition metal dichalcogenides. *Adv. Phys.* **1987**, *36*, 1−94.

(11) Wan, J.; Lacey, S. D.; Dai, J.; Bao, W.; Fuhrer, M. S.; Hu, L. Tuning two-dimensional nanomaterials by intercalation: materials, properties and applications. *Chem. Soc. Rev.* **2016**, *45*, 6742−6765.

(12) Hu, Z.; Wu, Z.; Han, C.; He, J.; Ni, Z.; Chen, W. Two-dimensional transition metal dichalcogenides: interface and defect engineering. *Chem. Soc. Rev.* **2018**, *47*, 3100−3128.

(13) Komsa, H.-P.; Kotakoski, J.; Kurasch, S.; Lehtinen, O.; Kaiser, U.; Krasheninnikov, A. V. Two-Dimensional Transition Metal Dichalcogenides under Electron Irradiation: Defect Production and Doping. *Phys. Rev. Lett.* **2012**, *109*, 035503.

(14) Yu, W.; Li, J.; Herng, T. S.; Wang, Z.; Zhao, X.; Chi, X.; Fu, W.; Abdelwahab, I.; Zhou, J.; Dan, J.; et al. Chemically Exfoliated VSe_2 Monolayers with Room-Temperature Ferromagnetism. *Adv. Mater.* **2019**, *31*, 1903779.

(15) Chua, R.; Yang, J.; He, X.; Yu, X.; Yu, W.; Bussolotti, F.; Wong, P. K. J.; Loh, K. P.; Breese, M. B. H.; Goh, K. E. J.; Huang, Y. L.; Wee, A. T. S. Can Reconstructed Se-Deficient Line Defects in Monolayer VSe_2 Induce Magnetism? *Adv. Mater.* **2020**, *32*, 2000693.

(16) Liu, Z.-L.; Lei, B.; Zhu, Z.-L.; Tao, L.; Qi, J.; Bao, D.-L.; Wu, X.; Huang, L.; Zhang, Y.-Y.; Lin, X.; Wang, Y.-L.; Du, S.; Pantelides, S. T.; Gao, H.-J. Spontaneous Formation of 1D Pattern in Monolayer VSe_2 with Dispersive Adsorption of Pt Atoms for HER Catalysis. *Nano Lett.* **2019**, *19*, 4897−4903.

(17) Wang, X.; Zhang, Y.; Si, H.; Zhang, Q.; Wu, J.; Gao, L.; Wei, X.; Sun, Y.; Liao, Q.; Zhang, Z.; et al. Single-atom vacancy defect to trigger high-efficiency hydrogen evolution of MoS_2. *J. Am. Chem. Soc.* **2020**, *142*, 4298−4308.

(18) Lin, J.; Pantelides, S. T.; Zhou, W. Vacancy-Induced Formation and Growth of Inversion Domains in Transition-Metal Dichalcogenide Monolayer. *ACS Nano* **2015**, *9*, 5189−5197.

(19) Liu, X.-C.; Zhao, S.; Sun, X.; Deng, L.; Zou, X.; Hu, Y.; Wang, Y.-X.; Chu, C.-W.; Li, J.; Wu, J.; Ke, F.-S.; Ajayan, P. M. Spontaneous self-intercalation of copper atoms into transition metal dichalcogenides. *Sci. Adv.* **2020**, *6*, No. eaay4092.

(20) Zhao, X.; Song, P.; Wang, C.; Riis-Jensen, A. C.; Fu, W.; Deng, Y.; Wan, D.; Kang, L.; Ning, S.; Dan, J.; et al. Engineering covalently bonded 2D layered materials by self-intercalation. *Nature* **2020**, *581*, 171−177.

(21) Wang, X.; Shen, X.; Wang, Z.; Yu, R.; Chen, L. Atomic-scale clarification of structural transition of MoS_2 upon sodium intercalation. *ACS Nano* **2014**, *8*, 11394−11400.

(22) Tan, S. J. R.; Abdelwahab, I.; Ding, Z.; Zhao, X.; Yang, T.; Loke, G. Z. J.; Lin, H.; Verzhbitskiy, I.; Poh, S. M.; Xu, H.; et al. Chemical stabilization of 1T′ phase transition metal dichalcogenides with giant optical Kerr nonlinearity. *J. Am. Chem. Soc.* **2017**, *139*, 2504−2511.

(23) Zhang, H.; Rousuli, A.; Zhang, K.; Luo, L.; Guo, C.; Cong, X.; Lin, Z.; Bao, C.; Zhang, H.; Xu, S.; et al. Tailored Ising superconductivity in intercalated bulk $NbSe_2$. *Nat. Phys.* **2022**, *18*, 1425−1430.

(24) Kanetani, K.; Sugawara, K.; Sato, T.; Shimizu, R.; Iwaya, K.; Hitosugi, T.; Takahashi, T. Ca intercalated bilayer graphene as a thinnest limit of superconducting C_6Ca. *Proc. Natl. Acad. Sci. U.S.A.* **2012**, *109*, 19610−19613.

(25) Lasek, K.; Coelho, P. M.; Zberecki, K.; Xin, Y.; Kolekar, S. K.; Li, J.; Batzill, M. Molecular Beam Epitaxy of Transition Metal (Ti-V-and Cr-) Tellurides: From Monolayer Ditellurides to Multilayer Self-Intercalation Compounds. *ACS Nano* **2020**, *14*, 8473−8484.

(26) Ma, Y.; Dai, Y.; Guo, M.; Niu, C.; Zhu, Y.; Huang, B. Evidence of the Existence of Magnetism in Pristine VX_2 Monolayers (X = S, Se) and Their Strain-Induced Tunable Magnetic Properties. *ACS Nano* **2012**, *6*, 1695−1701.

(27) Zhang, H.; Liu, L.-M.; Lau, W.-M. Dimension-dependent phase transition and magnetic properties of VS_2. *J. Mater. Chem. A* **2013**, *1*, 10821−10828.

(28) Isaacs, E. B.; Marianetti, C. A. Electronic Correlations in Monolayer VS_2. *Phys. Rev. B* **2016**, *94*, 035120.

(29) Zhuang, H. L.; Hennig, R. G. Stability and magnetism of strongly correlated single-layer VS_2. *Phys. Rev. B* **2016**, *93*, 054429.

(30) Mulazzi, M.; Chainani, A.; Katayama, N.; Eguchi, R.; Matsunami, M.; Ohashi, H.; Senba, Y.; Nohara, M.; Uchida, M.; Takagi, H.; Shin, S. Absence of nesting in the charge-density-wave system 1T-VS_2 as seen by photoelectron spectroscopy. *Phys. Rev. B* **2010**, *82*, 075130.

(31) Gauzzi, A.; Sellam, A.; Rousse, G.; Klein, Y.; Taverna, D.; Giura, P.; Calandra, M.; Loupias, G.; Gozzo, F.; Gilioli, E.; Bolzoni, F.; Allodi, G.; De Renzi, R.; Calestani, G. L.; Roy, P. Possible Phase Separation and Weak Localization in the Absence of a Charge-Density Wave in Single-Phase 1T-VS_2. *Phys. Rev. B* **2014**, *89*, 235125.

(32) Arnold, F.; Stan, R. M.; Mahatha, S. K.; Lund, H. E.; Curcio, D.; Dendzik, M.; Bana, H.; Travaglia, E.; Bignardi, L.; Lacovig, P.; et al. Novel Single-Layer Vanadium Sulphide Phases. *2D Mater.* **2018**, *5*, 045009.

(33) van Efferen, C.; Berges, J.; Hall, J.; van Loon, E.; Kraus, S.; Schobert, A.; Wekking, T.; Huttmann, F.; Plaar, E.; Rothenbach, N.; et al. A full gap above the Fermi level: the charge density wave of monolayer VS_2. *Nat. Commun.* **2021**, *12*, 6837.
(34) Coelho, P. M.; Nguyen Cong, K.; Bonilla, M.; Kolekar, S.; Phan, M.-H.; Avila, J.; Asensio, M. C.; Oleynik, I. I.; Batzill, M. Charge Density Wave State Suppresses Ferromagnetic Ordering in VSe_2 Monolayers. *J. Phys. Chem. C* **2019**, *123*, 14089−14096.
(35) Hardy, W. J.; Yuan, J.; Guo, H.; Zhou, P.; Lou, J.; Natelson, D. Thickness-Dependent and Magnetic-Field-Driven Suppression of Antiferromagnetic Order in Thin V_5S_8 Single Crystals. *ACS Nano* **2016**, *10*, 5941−5946.
(36) Niu, J.; Yan, B.; Ji, Q.; Liu, Z.; Li, M.; Gao, P.; Zhang, Y.; Yu, D.; Wu, X. Anomalous Hall effect and magnetic orderings in nanothick V_5S_8. *Phys. Rev. B* **2017**, *96*, 075402.
(37) Zhang, R.-Z.; Zhang, Y.-Y.; Du, S.-X. Thickness-dependent magnetic order and phase transition in V_5S_8. *Chin. Phys. B* **2020**, *29*, 077504.
(38) Nozaki, H.; Ishizawa, Y.; Saeki, M.; Nakahira, M. Electrical properties of V_5S_8 single crystals. *Phys. Lett. A* **1975**, *54*, 29−30.
(39) Moutaabbid, H.; Le Godec, Y.; Taverna, D.; Baptiste, B.; Klein, Y.; Loupias, G.; Gauzzi, A. High-Pressure Control of Vanadium Self-Intercalation and Enhanced Metallic Properties in 1T-$V_{1+x}S_2$ Single Crystals. *Inorg. Chem.* **2016**, *55*, 6481−6486.
(40) Bensch, W.; Koy, J. The single crystal structure of V_5S_8 determined at two different temperatures: anisotropic changes of the metal atom network. *Inorg. Chim. Acta* **1993**, *206*, 221−223.
(41) Niu, J.; Zhang, W.; Li, Z.; Yang, S.; Yan, D.; Chen, S.; Zhang, Z.; Zhang, Y.; Ren, X.; Gao, P.; et al. Intercalation of van der Waals layered materials: A route towards engineering of electron correlation. *Chin. Phys. B* **2020**, *29*, 097104.
(42) Zhou, Z.; Zhao, X.; Wu, L.; Liu, H.; Chen, J.; Xi, C.; Wang, Z.; Liu, E.; Zhou, W.; Pennycook, S. J.; et al. Dimensional crossover in self-intercalated antiferromagnetic V_5S_8 nanoflakes. *Phys. Rev. B* **2022**, *105*, 235433.
(43) Hall, J.; Pielić, B.; Murray, C.; Jolie, W.; Wekking, T.; Busse, C.; Kralj, M.; Michely, T. Molecular Beam Epitaxy of Quasi-Freestanding Transition Metal Disulphide Monolayers on van der Waals Substrates: A Growth Study. *2D Mater.* **2018**, *5*, 025005.
(44) Murray, C.; Jolie, W.; Fischer, J. A.; Hall, J.; van Efferen, C.; Ehlen, N.; Grüneis, A.; Busse, C.; Michely, T. Comprehensive Tunneling Spectroscopy of Quasifreestanding MoS_2 on Graphene on Ir(111). *Phys. Rev. B* **2019**, *99*, 115434.
(45) van Efferen, C.; Fischer, J.; Costi, T. A.; Rosch, A.; Michely, T.; Jolie, W. Modulated Kondo screening along magnetic mirror twin boundaries in monolayer MoS_2. *Nat. Phys.* **2024**, *20*, 82−87.
(46) Hall, J.; Ehlen, N.; Berges, J.; van Loon, E.; van Efferen, C.; Murray, C.; Rösner, M.; Li, J.; Senkovskiy, B. V.; Hell, M.; et al. Environmental Control of Charge Density Wave Order in Monolayer 2H-TaS_2. *ACS Nano* **2019**, *13*, 10210−10220.
(47) Knispel, T.; Berges, J.; Schobert, A.; van Loon, E. G. C. P.; Jolie, W.; Wehling, T.; Michely, T.; Fischer, J. Unconventional Charge-Density-Wave Gap in Monolayer NbS_2. *Nano Lett.* **2024**, *24*, 1045−1051.
(48) Castellanos-Gomez, A.; Buscema, M.; Molenaar, R.; Singh, V.; Janssen, L.; van der Zant, H. S. J.; Steele, G. A. Deterministic transfer of two-dimensional materials by all-dry viscoelastic stamping. *2D Mater.* **2014**, *1*, 011002.
(49) Kawada, I.; Nakano-Onoda, M.; Ishii, M.; Saeki, M.; Nakahira, M. Crystal structures of V_3S_4 and V_5S_8. *J. Solid State Chem.* **1975**, *15*, 246−252.
(50) Pielić, B.; Hall, J.; Despoja, V.; Rakić, I. Š.; Petrović, M.; Sohani, A.; Busse, C.; Michely, T.; Kralj, M. Sulfur Structures on Bare and Graphene-Covered Ir(111). *J. Phys. Chem. C* **2020**, *124*, 6659−6668.
(51) Kamber, U.; Pakdel, S.; Stan, R.-M.; Kamlapure, A.; Kiraly, B.; Arnold, F.; Eich, A.; Ngankeu, A. S.; Bianchi, M.; Miwa, J. A.; et al. Moiré-induced electronic structure modifications in monolayer V_2S_3 on Au (111). *Phys. Rev. B* **2021**, *103*, 115414.
(52) Komsa, H.-P.; Kurasch, S.; Lehtinen, O.; Kaiser, U.; Krasheninnikov, A. V. From Point to Extended Defects in Two-Dimensional MoS_2: Evolution of Atomic Structure Under Electron Irradiation. *Phys. Rev. B* **2013**, *88*, 035301.
(53) Lu, J.; Carvalho, A.; Chan, X. K.; Liu, H.; Liu, B.; Tok, E. S.; Loh, K. P.; Castro Neto, A. H.; Sow, C. H. Atomic Healing of Defects in Transition Metal Dichalcogenides. *Nano Lett.* **2015**, *15*, 3524−3532.
(54) Elibol, K.; Susi, T.; Argentero, G.; Reza Ahmadpour Monazam, M.; Pennycook, T. J.; Meyer, J. C.; Kotakoski, J. Atomic Structure of Intrinsic and Electron-Irradiation-Induced Defects in $MoTe_2$. *Chem. Mater.* **2018**, *30*, 1230−1238.
(55) Zhao, X.; Ji, Y.; Chen, J.; Fu, W.; Dan, J.; Liu, Y.; Pennycook, S. J.; Zhou, W.; Loh, K. P. Healing of Planar Defects in 2D Materials via Grain Boundary Sliding. *Adv. Mater.* **2019**, *31*, 1900237.
(56) Wong, P. K. J.; Zhang, W.; Bussolotti, F.; Yin, X.; Herng, T. S.; Zhang, L.; Huang, Y. L.; Vinai, G.; Krishnamurthi, S.; Bukhvalov, D. W.; et al. Evidence of Spin Frustration in a Vanadium Diselenide Monolayer Magnet. *Adv. Mater.* **2019**, *31*, 1901185.
(57) Murphy, D. W.; Cros, C.; Di Salvo, F. J.; Waszczak, J. V. Preparation and Properties of Li_xVS_2. *Inorg. Chem.* **1977**, *16*, 3027−3031.
(58) Bonilla, M.; Kolekar, S.; Li, J.; Xin, Y.; Coelho, P. M.; Lasek, K.; Zberecki, K.; Lizzit, D.; Tosi, E.; Lacovig, P.; Lizzit, S.; Batzill, M. Compositional Phase Change of Early Transition Metal Diselenide (VSe_2 and $TiSe_2$) Ultrathin Films by Postgrowth Annealing. *Adv. Mater. Interfaces* **2020**, *7*, 2000497.
(59) Nakano, M.; Wang, Y.; Yoshida, S.; Matsuoka, H.; Majima, Y.; Ikeda, K.; Hirata, Y.; Takeda, Y.; Wadati, H.; Kohama, Y.; Ohigashi, Y.; Sakano, M.; Ishizaka, K.; Iwasa, Y. Intrinsic 2D Ferromagnetism in V_5Se_8 Epitaxial Thin Films. *Nano Lett.* **2019**, *19*, 8806−8810.
(60) Meng, Q.; Zong, J.; Tian, Q.; Chen, W.; Xie, X.; Yu, F.; Qiu, X.; Wang, K.; Zhang, Y.; Wang, P.; Li, F.-S.; Wang, C.; Zhang, Y. Selectable Growth and Electronic Structures of Monolayer 1T-VSe_2 and V_5Se_8 Films on Bilayer Graphene. *Phys. Status Solidi RRL* **2022**, *16*, 2100601.
(61) Sumida, K.; Kusaka, S.; Takeda, Y.; Kobayashi, K.; Hirahara, T. Formation of monolayer V_5Se_8 from multilayer VSe_2 films via V- and Se-desorption. *Phys. Rev. B* **2022**, *106*, 195421.
(62) Ji, Q.; Li, C.; Wang, J.; Niu, J.; Gong, Y.; Zhang, Z.; Fang, Q.; Zhang, Y.; Shi, J.; Liao, L.; Wu, X.; Gu, L.; Liu, Z.; Zhang, Y. Metallic Vanadium Disulfide Nanosheets as a Platform Material for Multifunctional Electrode Applications. *Nano Lett.* **2017**, *17*, 4908−4916.
(63) Lee, S.-H.; Park, Y. C.; Chae, J.; Kim, G.; Kim, H. J.; Choi, B. K.; Lee, I. H.; Chang, Y. J.; Chun, S.-H.; Jung, M.; et al. Strong electron−phonon coupling driven charge density wave states in stoichiometric 1T-VS_2 crystals. *J. Mater. Chem. C* **2022**, *10*, 16657−16665.
(64) Ugeda, M. M.; Bradley, A. J.; Zhang, Y.; Onishi, S.; Chen, Y.; Ruan, W.; Ojeda-Aristizabal, C.; Ryu, H.; Edmonds, M. T.; Tsai, H. Z.; et al. Characterization of collective ground states in single-layer $NbSe_2$. *Nat. Phys.* **2016**, *12*, 92−97.
(65) Hou, X.-Y.; Zhang, F.; Tu, X.-H.; Gu, Y.-D.; Zhang, M.-D.; Gong, J.; Tu, Y.-B.; Wang, B.-T.; Lv, W.-G.; Weng, H.-M.; Ren, Z.-A.; Chen, G.-F.; Zhu, X.-D.; Hao, N.; Shan, L. Inelastic Electron Tunneling in 2H-$Ta_xNb_{1-x}Se_2$ Evidenced by Scanning Tunneling Spectroscopy. *Phys. Rev. Lett.* **2020**, *124*, 106403.
(66) Wen, C.; Xie, Y.; Wu, Y.; Shen, S.; Kong, P.; Lian, H.; Li, J.; Xing, H.; Yan, S. Impurity-pinned incommensurate charge density wave and local phonon excitations in 2H-NbS_2. *Phys. Rev. B* **2020**, *101*, 241404.
(67) Zhang, C.; Gong, C.; Nie, Y.; Min, K. A.; Liang, C.; Oh, Y. J.; Zhang, H.; Wang, W.; Hong, S.; Colombo, L.; Wallace, R. M.; Cho, K. Systematic study of electronic structure and band alignment of monolayer transition metal dichalcogenides in Van der Waals heterostructures. *2D Mater.* **2017**, *4*, 015026.
(68) Duvjir, G.; Choi, B. K.; Thi Ly, T.; Lam, N. H.; Jang, K.; Dung, D. D.; Chang, Y. J.; Kim, J. Multiple charge density wave phases of monolayer VSe_2 manifested by graphene substrates. *Nanotechnology* **2021**, *32*, 364002.
(69) Wang, Z.; Zhou, J.; Loh, K. P.; Feng, Y. P. Controllable phase transitions between multiple charge density waves in monolayer 1T-VSe_2 via charge doping. *Appl. Phys. Lett.* **2021**, *119*, 163101.

https://doi.org/10.1021/acsnano.3c05907
ACS Nano 2024, 18, 14161−14175

(70) Chua, R.; Henke, J.; Saha, S.; Huang, Y.; Gou, J.; He, X.; Das, T.; van Wezel, J.; Soumyanarayanan, A.; Wee, A. T. S. Coexisting Charge-Ordered States with Distinct Driving Mechanisms in Monolayer VSe_2. *ACS Nano* **2022**, *16*, 783−791.
(71) Fumega, A. O.; Diego, J.; Pardo, V.; Blanco-Canosa, S.; Errea, I. Anharmonicity Reveals the Tunability of the Charge Density Wave Orders in Monolayer VSe_2. *Nano Lett.* **2023**, *23*, 1794−1800.
(72) Liu, M.; Wu, C.; Liu, Z.; Wang, Z.; Yao, D.-X.; Zhong, D. Multimorphism and gap opening of charge-density-wave phases in monolayer VTe_2. *Nano Res.* **2020**, *13*, 1733−1738.
(73) Wu, Q.; Wang, Z.; Guo, Y.; Yang, F.; Gao, C. Orbital-collaborative charge density waves in monolayer VTe_2. *Phys. Rev. B* **2020**, *101*, 205105.
(74) van Gastel, R.; N'Diaye, A. T.; Wall, D.; Coraux, J.; Busse, C.; Buckanie, N. M.; Meyer zu Heringdorf, F. J.; Horn von Hoegen, M.; Michely, T.; Poelsema, B. Selecting a Single Orientation for Millimeter Sized Graphene Sheets. *Appl. Phys. Lett.* **2009**, *95*, 121901.
(75) Horcas, I.; Fernández, R.; Gómez-Rodríguez, J. M.; Colchero, J.; Gómez-Herrero, J.; Baro, A. M. W. S. X. M. WSXM: A software for scanning probe microscopy and a tool for nanotechnology. *Rev. Sci. Instrum.* **2007**, *78*, 13705.
(76) Preobrajenski, A.; Generalov, A.; Öhrwall, G.; Tchaplyguine, M.; Tarawneh, H.; Appelfeller, S.; Frampton, E.; Walsh, N. FlexPES: a versatile soft X-ray beamline at MAX IV Laboratory. *J. Synchrotron Radiat.* **2023**, *30*, 831−840.
(77) Hohenberg, P.; Kohn, W. Inhomogeneous electron gas. *Phys. Rev.* **1964**, *136*, B864−B871.
(78) Blöchl, P. E. Projector augmented-wave method. *Phys. Rev. B* **1994**, *50*, 17953−17979.
(79) Kresse, G.; Hafner, J. Ab initio molecular dynamics for liquid metals. *Phys. Rev. B* **1993**, *47*, 558−561.
(80) Kresse, G.; Furthmüller, J. Efficient iterative schemes for ab initio total-energy calculations using a plane-wave basis set. *Phys. Rev. B* **1996**, *54*, 11169−11186.
(81) Kohn, W.; Sham, L. J. Self-consistent equations including exchange and correlation effects. *Phys. Rev.* **1965**, *140*, A1133−A1138.
(82) Lee, K.; Murray, É. D.; Kong, L.; Lundqvist, B. I.; Langreth, D. C. Higher-accuracy van der Waals density functional. *Phys. Rev. B* **2010**, *82*, 081101.
(83) Becke, A. On the large-gradient behavior of the density functional exchange energy. *J. Chem. Phys.* **1986**, *85*, 7184−7187.
(84) Hamada, I. van der Waals density functional made accurate. *Phys. Rev. B* **2014**, *89*, 121103.
(85) Huttmann, F.; Martínez-Galera, A. J.; Caciuc, V.; Atodiresei, N.; Schumacher, S.; Standop, S.; Hamada, I.; Wehling, T. O.; Blügel, S.; Michely, T. Tuning the van der Waals Interaction of Graphene with Molecules via Doping. *Phys. Rev. Lett.* **2015**, *115*, 236101.
(86) Perdew, J. P.; Burke, K.; Ernzerhof, M. Generalized gradient approximation made simple. *Phys. Rev. Lett.* **1996**, *77*, 3865−3868.

https://doi.org/10.1021/acsnano.3c05907
ACS Nano 2024, 18, 14161−14175